

Machine learning-based lifelong estimation of lithium plating potential: A path to health-aware fastest battery charging

Abstract

To enable a shift from fossil fuels to renewable and sustainable transport, batteries must allow fast charging and exhibit extended lifetimes—objectives that traditionally conflict. Current charging technologies often compromise one attribute for the other, leading to either inconvenience or diminished resource efficiency in battery-powered vehicles. For lithium-ion batteries, the way to meet both objectives is for the lithium plating potential at the anode surface to remain positive. In this study, we address this challenge by introducing a novel method that involves real-time monitoring and control of the plating potential in lithium-ion battery cells throughout their lifespan. Our experimental results on three-electrode cells reveal that our approach can enable batteries to charge at least 30% faster while almost doubling their lifetime. To facilitate the adoption of these findings in commercial applications, we propose a machine learning-based framework for lifelong plating potential estimation, utilizing readily available battery data from electric vehicles. The resulting model demonstrates high fidelity and robustness under diverse operating conditions, achieving a mean absolute error of merely 3.37 mV. This research outlines a practical methodology to prevent lithium plating and enable the fastest health-conscious battery charging.

Keywords: Lithium-ion battery, lithium plating potential estimation, fast charging, data-driven models, machine learning.

1. Introduction

At the forefront of a transition to sustainable mobility are lithium-ion (Li-ion) batteries, because of their high energy density, cost-effectiveness, and durability, establishing themselves as the primary power source for electric vehicles (EVs) [1, 2, 3, 4]. Yet, as the industry strives to match the convenience of traditional fueling methods, it encounters significant hurdles in fast-charging technology that do not compromise battery lifespan [5].

Rapid charging introduces a dilemma; on the one hand, it necessitates high current levels, leading to excessive heat generation that, if not adequately dissipated through advanced thermal management systems, can significantly accelerate several battery aging mechanisms, such as solid electrolyte interface (SEI) growth [6, 7]. On the other, even when thermal issues are addressed, the escalated current can trigger intricate mechanical and electrochemical reactions within the battery, further exacerbating its degradation [8]. These challenges have catalyzed a plethora of research aimed at developing fast-charging strategies while protecting the health of the battery [9, 10].

Among the myriad of factors influencing battery degradation during fast charging, lithium plating emerges as a

critical concern [10, 11, 12]. This phenomenon—characterized by the deposition of metallic lithium on the anode’s surface—directly undermines the battery’s capacity and efficiency by reducing the cyclable lithium and impeding the normal intercalation process. The consensus among researchers is that lithium plating needs to be prevented for prolonged battery life and maintained performance during rapid charging [13, 14, 15, 16]. Recent studies have demonstrated that the microstructural inhomogeneities in graphite electrodes significantly influence the onset and severity of lithium plating, necessitating the refinement of both electrode design and charging protocols [17]. Despite a well-established theoretical foundation for regulating the plating potential to mitigate this issue [5, 13, 18], empirical validation and practical application of such strategies, especially over the battery’s lifespan, remain limited.

Methods to extract the information of plating potential can be categorized into three groups, including direct/indirect measurements, model-based methods, and data-driven methods [5, 8]. The most straightforward approach involves inserting a lithium metal reference electrode between the negative electrode and separator of a battery cell to enable the measurement of the anode voltage during battery operation [18, 19]. However, the insertion of such reference electrodes can be practically challenging due to the incurred additional costs and space requirements, making it unfeasible for any cost- and energy-density-sensitive applications. Moreover, the normal electrochemical reaction may be affected by the inserted reference electrode, for example, by blocking certain areas for Li-ion intercalation and deintercalation [20, 21]. Last but not least, if lithium metal was used as the reference electrode, the extra lithium added to the cell may participate in the charge and discharge reactions, potentially altering the cell’s behavior compared to a normal cell without reference electrodes.

Using a high-fidelity model to estimate the detailed internal battery states is another way to capture the plating potential information during battery usage. Lu *et al.* [22] constructed an equivalent circuit model (ECM) and used an extended Kalman filter to estimate the plating potential. However, due to the coupled effect of the cathode and anode, the plating potential may become unidentifiable. Another commonly employed class of model for such an estimation task is physics-based models, such as the pseudo-two-dimensional (P2D) model [23]. In contrast to the ECM, which only captures the battery’s lumped electric behavior, the P2D model uses the porous electrode and concentrated solution theory to simulate the internal electrochemical reactions, which can predict the plating potential’s evaluation in response to external operating conditions. Based on the P2D model coupled with thermal dynamics, Ringback *et al.* [24] designed an observer to estimate the plating potential together with its lower bound in the presence of model uncertainties. Compared to employing the full-order electrochemical model, which requires an excessive amount of computational power and a complex solver to solve the partial differential-algebraic equations (PDAE), control-oriented models that require light computation while capturing key battery dynamics are desired. Following this trend, Li *et al.* [25] designed an observer for the plating potential based on the single particle model (SPM). The SPM can achieve reasonable accuracy at low to moderate current rates but lose fidelity at high currents. Additionally, to successfully use physics-based models, it is essential to have accurate parameters. However, identifying a large set of parameters over various battery operation conditions, e.g., different state of charge (SoC) levels, current profiles, temperatures, and different health levels, remains an open research question [26, 27]. Moreover, even with a reliable

and simplified electrochemical model, running it for every battery cell is still computationally challenging, considering the targeted applications often contain hundreds or even thousands of cells.

Due to the ever-increasing awareness of collecting battery operation data and employing the concept of cloud battery management systems (BMS) to access much higher computational power, data-driven methods have gained popularity in dealing with battery diagnosis and prognosis. With sufficiently large and high-quality datasets, data-driven methods often demonstrate excellent performance in estimating or predicting battery SoC, state of health (SoH), and remaining useful life (RUL) [28, 29, 30, 31]. In this regard, data-driven methods can be a good candidate, whereas there are very limited attempts to estimate battery plating potential and avoid the onset of lithium plating during charging. Lin [32] adopted a long short-term memory neural network (LSTM) to estimate the plating potential using synthetic data generated from a physics-based battery model. However, only limited operating conditions were considered, e.g., the constant current charging, standard driving profiles, and short time horizon, which may hinder the model's applicability. Hamar *et al.* [33] further extended the work to incorporate more realistic operating conditions with different cycling temperatures, various initial SoC levels, and multi-step constant charging. Nonetheless, under the same charging conditions repeated over different cycles, the plating potential can be significantly affected by how the battery has aged [14, 18]. In fact, old batteries are more prone to trigger lithium plating. Therefore, it is crucial to consider the impact of battery aging on the plating potential. To the best of our knowledge, there is no established work capable of accurately and online estimating the plating potential over the battery's entire life.

Our study aims to combine theoretical insights with practical applications in the fast charging of batteries, driven by two principal innovations. First, we validate the effectiveness of a plating potential controlled charging method using three-electrode battery cells, demonstrating marked improvements in both battery lifetime and charging rate over conventional methods. Building upon this foundation, we then develop an innovative ML-based framework for the lifelong estimation of battery plating potential, thus avoiding the three-electrode setup. This framework utilizes real-time measurements to learn electrochemical behaviors on a fast timescale alongside online estimated SoH indicators for which the effect of aging on plating potential has been learned. Comprehensive validation of this framework through extensive battery cycling data under diverse operating conditions and aging levels demonstrates its robustness and accuracy. These innovations collectively represent a significant stride towards health-aware, fast-charging solutions for EV batteries.

2. Results and discussion

2.1. Three-electrode cell experiments

In the experimental setup, the EL-CELL PAT-Cell was used for testing three-electrode cells, as illustrated in Fig. 1a and b. For the three-electrode cells, Nickle Manganese Cobalt (NMC) oxides of type 811 were used as the positive electrode, and artificial graphite was used as the negative electrode, both supplied by Customcells Itzehoe GmbH. Detailed specifications of the electrode materials are available in the *Supplemental Information* (i.e., Note 4). All the

cell assembling operations were carried out in an argon-filled glove box. First, the electrode sheets were die-cut to a coin size with a diameter of 18 mm. Then, the positive electrode, the negative electrode, and the separator were assembled into the PAT-Cell stack. Borosilicate glass fiber separators (260 μm , Whatman FG/A) were used, in which a lithium metal ring served as a reference electrode to measure the electrode potential during battery operation. The electrolyte used was a 90 μL lithium hexafluorophosphate solution in a mixture of ethylene carbonate and dimethyl carbonate (LiPF₆ LP50). The nominal capacity of the assembled three-electrode cells is 5 mAh, which is used as the basis when defining C-rates in subsequent test instructions.

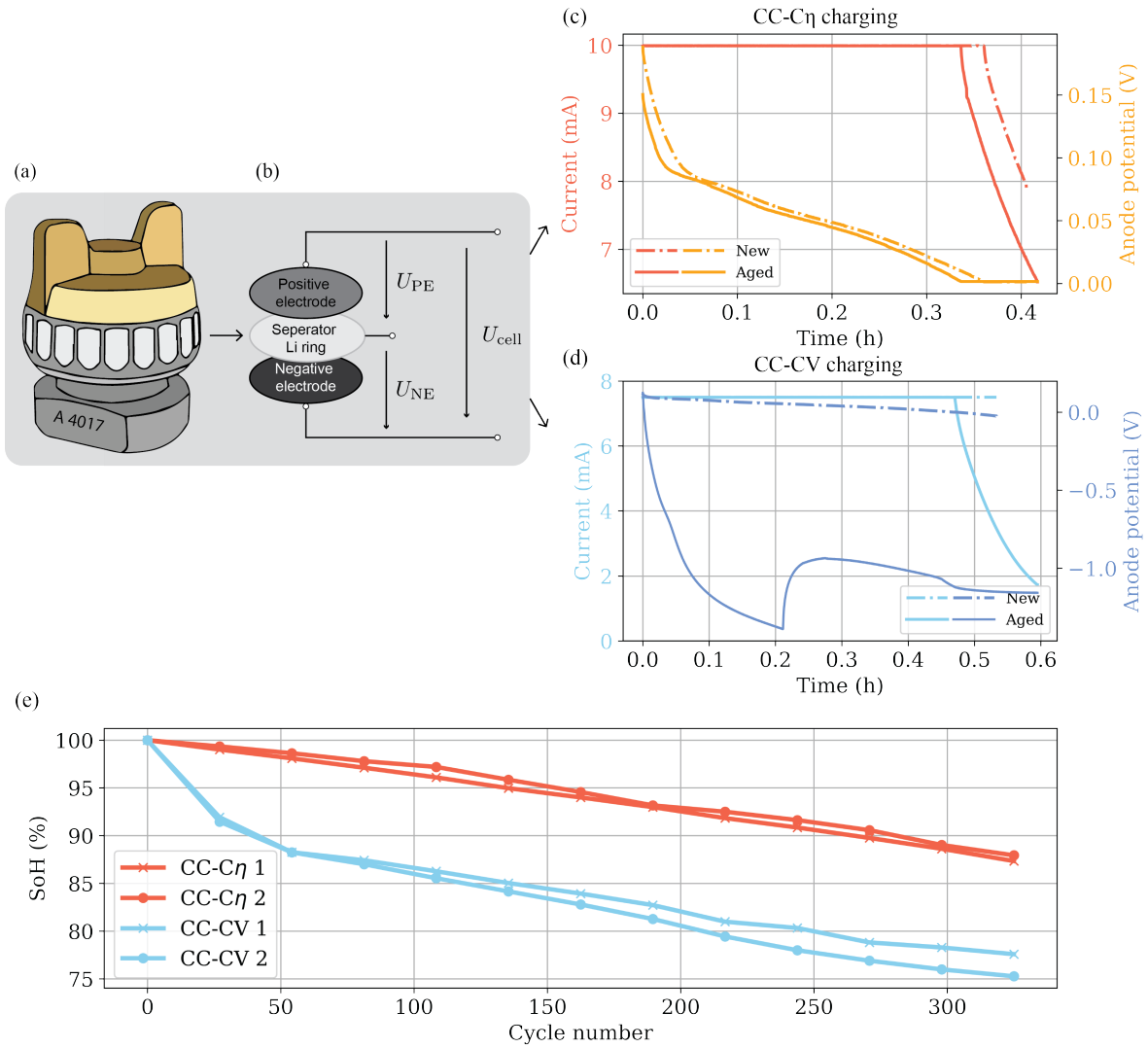


Figure 1: The three-electrode cell test setup used for experiments. (a) shows the EL-cell three-electrode cell holder. (b) illustrates the internal structure of the cell and the measured signals, including the cell voltage U_{cell} and the anode voltage U_{NE} . (c) illustrates the current and anode potential profiles of a studied cell at different aging levels and under CC-C η charging. (d) illustrates the current and anode potential profiles of another studied cell under CC-CV charging. (e) presents the aging curves of four cells experiencing the two different charging strategies.

The experimental procedures were carried out in a controlled temperature chamber (ESPEC LHU-124), utilizing the PAT-Stand-1 cell holder, and subjected to cycling using a NEWARE coin cell cycler. The temperature chamber was maintained at a constant temperature of 25°C. After the assembly of the cells, a formation cycle was executed following the guidelines provided by Customcells. The formation cycle profile was first, according to Profile 1, repeated twice as listed in Table 1, then following Profile 2, repeated twice. To assess the aging status of the battery cells, reference performance tests (RPTs) were scheduled every 25 normal cycles. During these tests, Profile 3 was executed twice, and the average value of the two discharge capacities was defined as the cell's reference capacity.

Table 1: CC-CV charging and CC discharging profiles for the designed three-electrode cell experiment.

		Charge phase			Discharge phase	
		Current	Voltage limit	Cut-off condition	Current	Voltage limit
CC-CV	Profile 1	0.1C	4.2V	1/25C	0.1C	3V
	Profile 2	0.2C	4.2V	1/25C	0.2C	3V
	Profile 3	1C	4.2V	1/10C	1C	3V
	Profile 4	1.5C	4.2V	1/10C or 4 mAh	1C	3V
CC- $C\eta$	Profile 5	2C	4.5V	4 mAh	1C	3V

In this study, a total of four cells were assembled and used in the experimental campaign. Two of the cells served as a reference group, undergoing constant current-constant voltage (CC-CV) charging according to Profile 4 in Table 1. The charging process for these cells was terminated when the current met 0.1C or the accumulated charged capacity reached 4 mAh, which is equivalent to 80% of the nominal capacity (see Fig. 1d). The remaining two cells were operated under a lithium-plating-free charging strategy, wherein the charging current was controlled to maintain non-negativity of the plating potential (η), i.e. ensuring $\eta > 0$. A safety margin of 1 mV is applied to account for the potential variability of the plating potential measurement. Designated as Profile 5 and referred to as CC- $C\eta$ charging, this approach constituted the experimental group for advanced comparative analysis (depicted in Fig. 1c). Here, a higher current value was adopted in the CC stage for CC- $C\eta$ charging compared to CC-CV, ensuring that the two strategies have comparable charging durations. This arrangement facilitates a direct comparison of their effects on battery degradation. For all the defined tests, we measured and collected data on current, voltage, temperature, and plating potential at a sampling frequency of 1 Hz.

The rationale for maintaining a positive plating potential ($\eta > 0$) to prevent the initiation of lithium plating is grounded in equilibrium thermodynamics principles [15, 34, 35, 36], which are used to explain when lithium plating begins. According to this theoretical framework, lithium plating becomes thermodynamically favorable when the potential of the graphite electrode falls below 0 V versus Li/Li⁺. This situation may arise if the intercalation reaction experiences significant kinetic limitations, leading to a large overpotential. This overpotential can surpass the equilibrium potential of the lithium-graphite phase diagram, consequently causing the graphite potential to drop

below 0 V versus Li/Li⁺. While this voltage criterion alone is not sufficient to guarantee lithium plating, it is a necessary condition for its occurrence [37, 38]. Thus, from a practical application perspective, using this criterion is both feasible and advantageous for mitigating lithium plating.

2.2. Synthetic data generation

To cover wide operating conditions and diverse aging trajectories that batteries may encounter in real-world applications, synthetic data was generated by simulating a single particle model, including electrolyte dynamics (SPMe), and coupled with several aging mechanisms. The modeling of battery aging is an active research area. So far, there is no universally accepted model that covers all aging mechanisms possibly triggered in typical Li-ion batteries. In this regard, three major aging mechanisms are considered in the simulations, including SEI layer growth in the anode and loss of active materials in the anode and cathode [39]. For a more detailed introduction to the employed SPMe-aging model, readers are referred to the literature works [40, 41, 39]. It is worth mentioning that apart from these three aging mechanisms, lithium plating is also known as one of the major aging mechanisms during the usage of Li-ion batteries, particularly at high charging currents, low temperatures, high SoC levels, and in aged cells [42, 43]. However, since this study eventually aims to develop a fast-charging strategy capable of keeping the plating potential positive to prevent lithium plating, we do not consider it in the simulation model.

By varying aging-related parameters sequentially, the above battery model was simulated extensively on the platform PyBaMM [44] under a wide range of operating conditions (as detailed in Section 4.1.3). The simulations that were conducted resulted in a large synthetic dataset consisting of two parts. One part of the dataset includes time-series data of current, voltage, temperature, and plating potential recorded at a sampling rate of 1 Hz. The other part contains four SoH indicators, i.e., the battery capacity, lithium inventory loss (LLI), loss of active materials in the negative electrode (LAM_{NE}), and loss of active material in the positive electrode (LAM_{PE}), recorded at the end of each RPT cycle. To partially visualize the dataset, the generated 1,392 aging trajectories are depicted in Fig. S1 (see *Supplemental Information*). With the end of life defined at 80% of the nominal capacity, it can be seen that the battery lifetimes corresponding to the different parameter settings span from 20 to 2000 cycles. Further details for the employed battery model and its implementation are introduced in Section 4.1.

2.3. Lifelong estimation framework for plating potential

In this study, we introduce an innovative framework designed for the lifelong estimation of plating potential, as illustrated in Fig. 2. Central to our approach are two pivotal tasks executed through the integration of three ML models. Specifically, the framework employs two slow timescale models (Model 1 and Model 2) for estimating the battery's capacity and the three aging modes both on a slow timescale and Model 3 for estimating the plating potential on a fast timescale. This structured framework leverages the strengths of each model to deliver an accurate, robust, and real-time estimation of the plating potential over the battery's lifespan.

For Model 1, the inputs, also called features, are manually constructed from time-series and histogram-based raw data, e.g., the slope of the voltage curves and the accumulated energy throughput. The output of this model is battery capacity. For Model 2, the inputs include time-series current, voltage, and temperature measurements, while the outputs are the three aging modes (namely LLI, LAM_{PE}, and LAM_{NE}). Considering the nature of slow aging dynamics, we develop Model 1 and Model 2 from the data collected during RPT tests, which, as specified in Section 2.1, were conducted every 25 normal cycles. For real-world vehicle applications, the data samples for training these two ML models can be collected during destination charging, in which the charging current is low (often lower than 1/8C). This provides beneficial conditions, such as wide SoC ranges, relatively stable temperatures, and mild lithium diffusion processes, for extracting high-quality data samples. To label the four SoH indicators as the model output, the battery capacity can be calibrated according to Profile 3 of Section 2.1, and the three aging modes are calculated from the open-circuit voltage (OCV), as introduced in Note 1 of the *Supplemental Information*.

With the plating potential as the unique output, Model 3 has two types of inputs. The first type of input comprises time-series current, voltage, and temperature measurements, from which we aim to learn the fast battery dynamics. As the ultimate target is to optimize battery charging performance in real-time, the input data could be extracted from the corresponding fast charging profile. The second type is the four outputs from Model 1 and Model 2, by which we inform Model 3 of the battery health characteristics. Essentially, Model 3 combines time-series and non-temporal features to adaptively estimate the plating potential over the battery’s entire lifetime. To pave the way for later conservative fast-charging control implementation, an underestimated plating potential result is preferred compared to an overestimate. We therefore propose an underestimate-enhanced long short-term memory (UE-LSTM) to refine the precision of plating potential estimations while inherently biasing towards underestimations. The idea is to ensure prediction accuracies but with a preference for conservative estimates.

In the proposed framework, the three ML models operate in parallel. At low current rates, such as those encountered during destination charging, the risk of lithium plating diminishes, reducing the necessity for real-time plating potential estimation. In such circumstances, it may be unnecessary to activate Model 3. Conversely, during fast charging, precise estimation of the plating potential becomes critical to prevent lithium plating, highlighting the critical role of Model 3. It is worth mentioning that this framework can be seamlessly integrated with existing vehicle BMS, utilizing readily available measurements to enable onsite quantification of all the SoH indicators and real-time estimation of the plating potential.

2.4. Results of the three-electrode cell test

By implementing the experiments designed in Section 2.1, the aging trajectories of all the studied battery cells can be obtained, as depicted in Fig. 1e. To the best of our knowledge, these are the first published experimental results that directly measure the plating potential and use it to dynamically control the charging current in a closed-loop fashion during the battery’s lifelong operation. It can be seen that at the end of the test, corresponding to 325 normal cycles, both cells in the CC-CV group had passed their end of life, with a SoH below 80%. Specifically, these cells

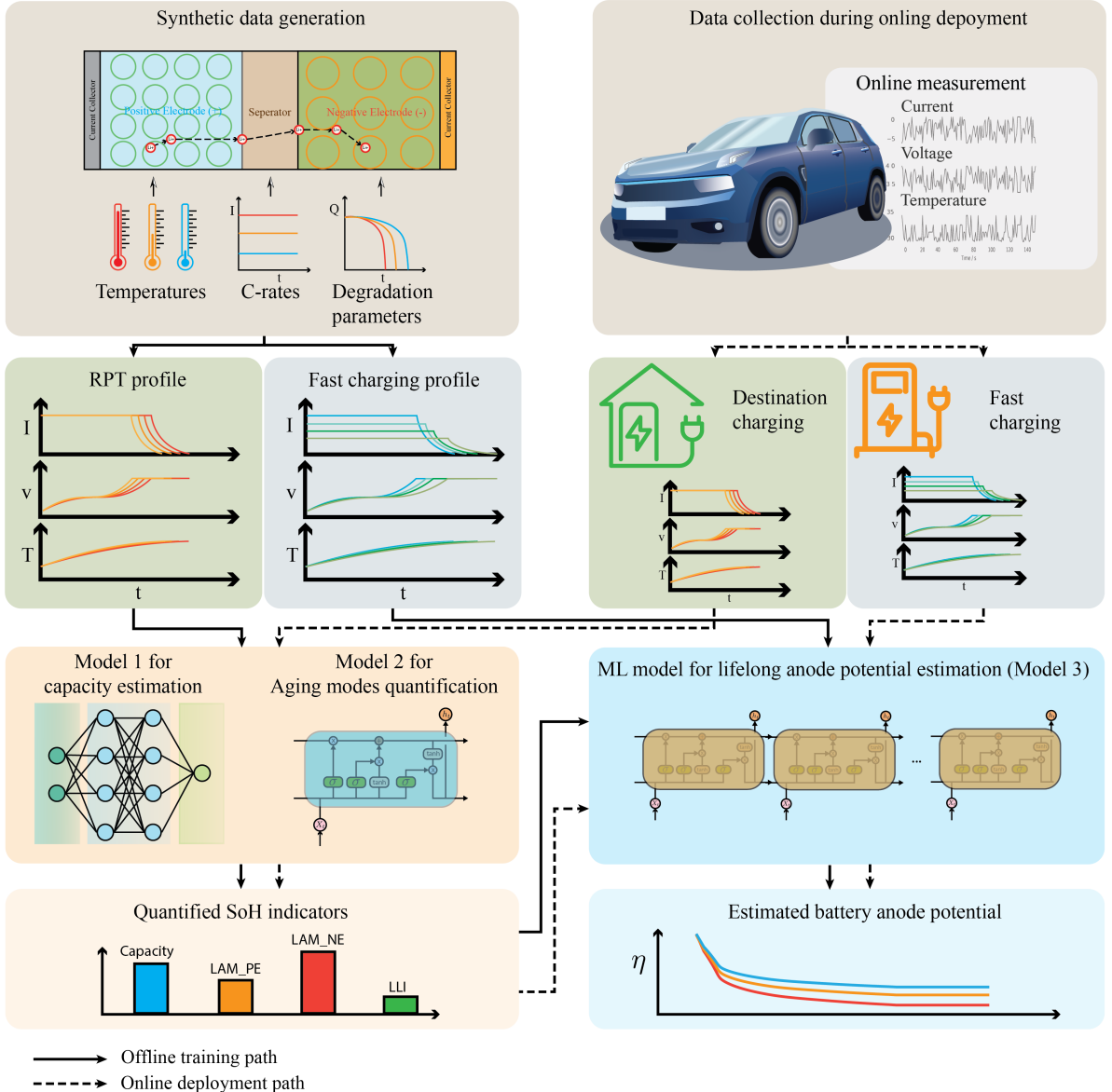


Figure 2: The proposed framework for lifelong estimation of battery plating potential.

suffered from a sharp capacity loss, i.e., 12% of the nominal capacity, within the first 50 cycles, attributed to the onset of lithium plating, as evidenced by the negative plating potential shown in Fig. 1d. In contrast, the two cells in the CC- $C\eta$ group were able to retain an SoH above 87% beyond the 325th cycle, suggesting a markedly extended lifespan compared to their counterparts. This improvement is derived from the CC- $C\eta$ charging strategy continuously monitoring the plating potential and ensuring its non-negativity.

Beyond extending battery lifetime, the CC- $C\eta$ charging strategy significantly surpassed CC-CV charging in terms of efficiency. It also achieves a 30% initial reduction in charging time and a 40% reduction by the 200th cycle, as

illustrated in Fig. 1c–d.

The above experimental results demonstrate that real-time control of the charging profile based on the plating potential (η) can significantly extend battery lifetime while enabling faster charging. These findings not only confirm the viability of health-aware fastest charging but also point out how to achieve it. It strongly motivates the lifelong estimation of η in Section 2.3, given it is not economically feasible to incorporate reference electrodes into each commercial battery.

Conventionally, the evaluation of a given charging strategy with respect to battery degradation and lifetime relies heavily on extensive experiments over thousands of cycles, especially considering diverse operating conditions. As per the results in Fig. 1, the long-term effects of different charging strategies on battery health can be largely revealed by the profile of η in the early cycling stage, thus significantly mitigating the need for extremely time-consuming and expensive experiments. This benefit will, in turn, accelerate the improvement and optimization process of existing battery materials and design for faster charging and a longer lifetime.

2.5. Estimation results for SoH indicators

The results for the estimation of the four SoH indicators using Model 1 and Model 2 applied to the full SoC operating window are presented in Fig. 3a and the two first rows of Table 2. The models exhibit high estimation fidelity for all the SoH indicators, achieving a mean absolute error (MAE) below 0.4% and a root-mean-square error (RMSE) below 0.55%. The estimation accuracy is slightly lower in LAM_{NE} compared to LAM_{PE}. However, although the estimation of LAM_{NE} results in the highest average error among all the indicators, the absolute error remains within 1.07% for 95% of the test dataset, underscoring the model's high accuracy and robustness across a broad spectrum of operating conditions. The relatively reduced accuracy in LAM_{NE} estimations, as compared to LAM_{PE}, may be attributed to the more flat open-circuit potential (OCP) of the anode compared to that of the cathode, which complicates the discernment of LAM_{NE} variations via the cell's current and voltage. This observation aligns well with previous findings in [45].

For the training of our ML algorithms, we extensively varied aging-related parameters in the simulation to generate a large and diverse synthetic dataset. For further examination, we randomly select a simulated battery cell from the dataset. The estimation trajectories for each SoH indicator over the cell's entire lifetime are shown in Fig. 3b. As can be seen, the estimates closely follow the calibrated values, with maximum estimation errors staying well within the $\pm 2.5\%$ error bounds. This verifies the prediction capability of our developed Models 1 and 2. It is important to note that the randomly selected simulated cell, exhibiting nearly linear SoH indicator trajectories, is a special case. Among the 1,392 simulated aging trajectories, the aging behavior of other cells varies significantly. As illustrated in Fig. S1 (see *Supplemental Information*), many cells demonstrate distinct patterns of capacity degradation, with clear non-linear characteristics. Similarly, the SoH indicators exhibit pronounced non-linearity over the cycle life, as visualized in Fig. S2. To underscore the necessity of employing the proposed non-linear model, we benchmark it against two linear models for estimating the SoH indicators. The results from these comparisons strongly indicate

that a non-linear approach is crucial for accurately capturing the complex aging behavior of batteries. A detailed comparison of the results is provided in Tables S3 and S4 (see *Supplemental Information*).

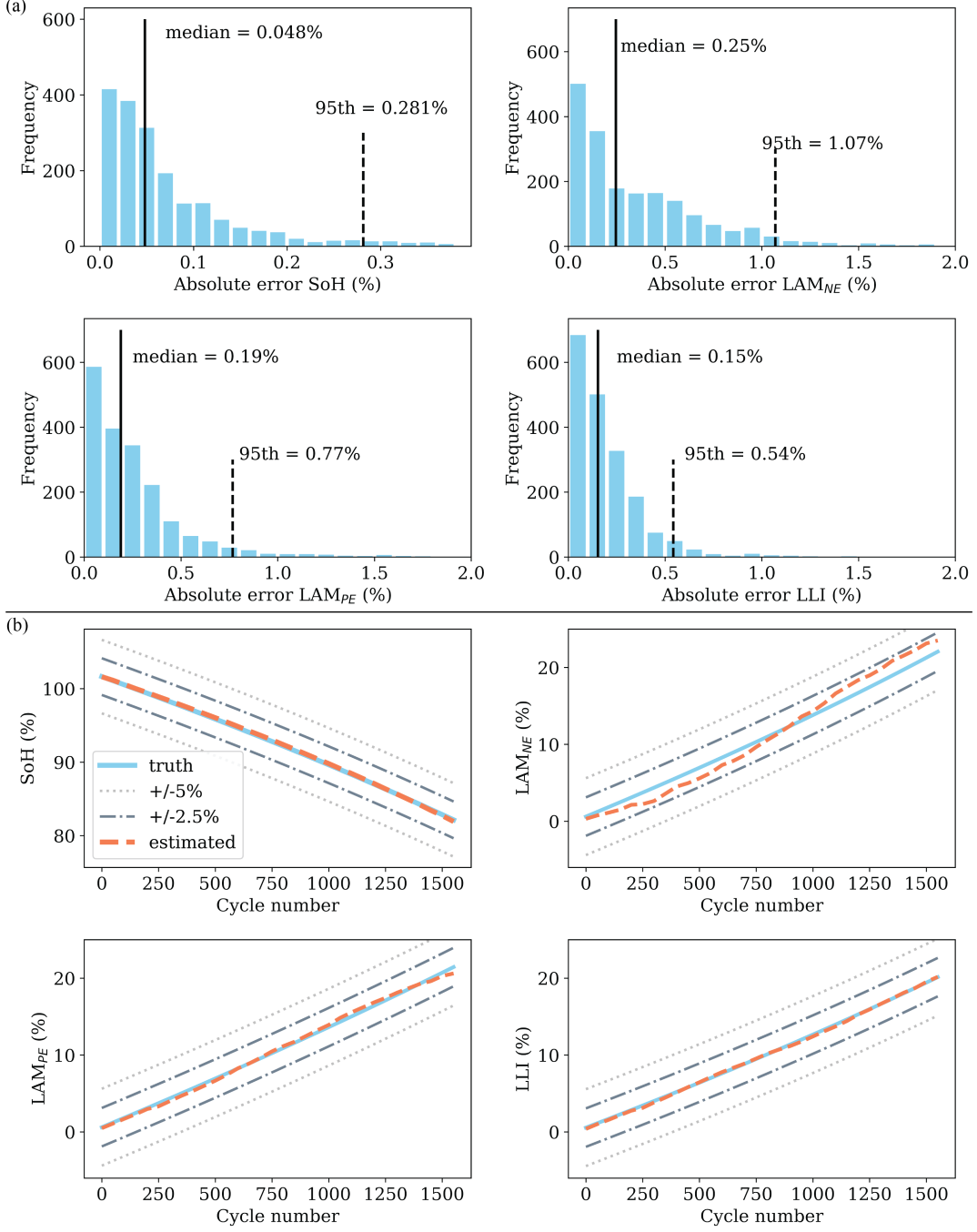


Figure 3: Estimation results of the four SoH indicators for batteries operated under the full SoC window. (a) displays the histogram results for all data samples in the test set. For a randomly selected ‘cell’ from the simulation pool, (b) presents the estimated trajectories against their ground truth along the equivalent full cycles.

In real-world vehicular applications, battery discharge and charge cycles rarely span the full 0–100% SoC window. Instead, batteries typically undergo various partial charging cycles, including the aforementioned destination charging for EVs. Such a context necessitates a comprehensive evaluation of the developed ML models for SoH indicator quantification under realistic charging conditions. Accordingly, we assess the performance of Model 1 and Model 2 across six distinct usage scenarios, each characterized by a unique SoC window. Table 2 presents the estimation errors for the four SoH indicators across these scenarios. Despite a slight reduction in accuracy relative to the full SoC window scenario, the obtained estimates maintain high reliability, with average errors remaining below 1% for all the scenarios and SoH indicators. These results point to the real-world applicability of Model 1 and Model 2 as used in the proposed estimation framework. Note 6 of the *Supplemental Information* provides more results regarding the overall estimation errors under different usage conditions.

Table 2: Estimation results for battery SoH indicators under different charging scenarios.

SoC window (%)		SoH capacity (%)	LAM _{NE} (%)	LAM _{PE} (%)	LLI (%)
0–100	MAE	0.077	0.375	0.269	0.200
	RMSE	0.131	0.546	0.439	0.289
20–50	MAE	0.335	0.458	0.268	0.232
	RMSE	0.429	0.702	0.421	0.370
30–60	MAE	0.357	0.603	0.344	0.241
	RMSE	0.554	0.777	0.887	0.872
40–70	MAE	0.431	0.470	0.451	0.312
	RMSE	0.719	0.789	0.641	0.432
50–80	MAE	0.389	0.580	0.633	0.398
	RMSE	0.610	0.880	0.982	0.586
60–90	MAE	0.335	0.557	0.393	0.255
	RMSE	0.429	0.859	0.673	0.408
70–100	MAE	0.099	0.544	0.385	0.161
	RMSE	0.165	0.956	0.578	0.245

2.6. Estimation results for lifelong plating potential

1) Noise specification for model training. In the development of Model 3, we have meticulously accounted for uncertainties inherent to the estimation of SoH indicators and the measurement of current, voltage, and temperature encountered in real-world applications. This is achieved by augmenting the training dataset with Gaussian white noise, thereby simulating the influence of estimation and measurement inaccuracies on model training. For all four SoH indicators, the noise is calibrated based on the most challenging real-world conditions, using the largest RMSE

observed across the six partial charging scenarios (as highlighted in Table 2) to define the standard deviation of the Gaussian noise. The choice of measurement noise for current, voltage, and temperature is based on the specifications and experience of widely utilized battery sensor technologies. Specifically, we used the sensor noise with standard deviations corresponding to Level 4 defined in Table 4 as the default.

2) The overall performance of Model 3. Our examination of the plating potential estimation, as delineated in Fig. 4, reveals that Model 3 is capable of predicting the battery's plating potential with a high degree of accuracy over the entire lifespan, limiting the maximum error to less than 20 mV. This precision is further highlighted in the zoomed-in section of Fig. 4a, where the cumulative error histogram demonstrates that 95% of the estimations maintain an absolute error below 10 mV. Further quantitative analysis, represented in the last row of Table 3, showcases that the model has an MAE of 3.37 mV and an RMSE of 4.77 mV. These values affirm the model's high fidelity and robustness in estimating the plating potential across diverse operating conditions.

A detailed case study, illustrated in Fig. 4c, tracks the plating potential estimation for a randomly selected cell throughout its lifespan. The performance in estimating plating potentials near 0 V, essential for optimizing battery charging performance, is highlighted in the zoomed-in figure. This in-depth analysis reveals the model's capacity to not only closely follow the cell's true trajectory of plating potential but also adapt dynamically to its aging status.

3) The effect of different SoH indicators. Four established SoH indicators have been integrated into the feature set of Model 3. To study the importance of the individual SoH indicators for plating potential estimation. We change the number of SoH indicators utilized inside the model, resulting in four alternative models characterized by their inputs, where Model 3a utilizes only the directly measured current, voltage, and temperature (see Table 3 for details).

It is observed from Table 3 and Fig. 4b that with an increasing number of SoH indicators added to the feature set, the model accuracy is consistently improved, regardless of the number of data samples tested. Furthermore, leveraging the full array of SoH indicators, Model 3 outperforms all its counterparts that lack equally comprehensive aging information. In comparison to Model 3a, Model 3 achieves a reduction in the MAE and RMSE by 22% and 24%, respectively. This enhancement in predictive accuracy demonstrates the importance of including detailed information on battery capacity and aging modes within the estimation framework.

4) The effect of different ML models. To evaluate the effectiveness of our proposed UE-LSTM in the development of Model 3, we implemented three alternative ML algorithms for comparison: the gated recurrent unit (GRU) neural network, an artificial neural network (ANN), and Transformer (see Section 4.2.4 for details).

The comparative analysis between LSTM and UE-LSTM is illustrated in Fig. 4d–e. Although the overall performance in estimation accuracy of these two algorithms is similar, a notable distinction is observed in the nature of the estimation errors. Specifically, 56% of the estimation errors generated by the UE-LSTM are attributable to underestimation, marking a 7% increase compared to the conventional LSTM. This underestimation characteristic of UE-LSTM implies a potential for providing larger safety margins in the design of control strategies based on the estimated plating potential. Additional comparative results, particularly against GRU, ANN, and Transformer models, are available in Note 3 of the *Supplemental Information*. These results further attest to the UE-LSTM's superior

estimation accuracy.

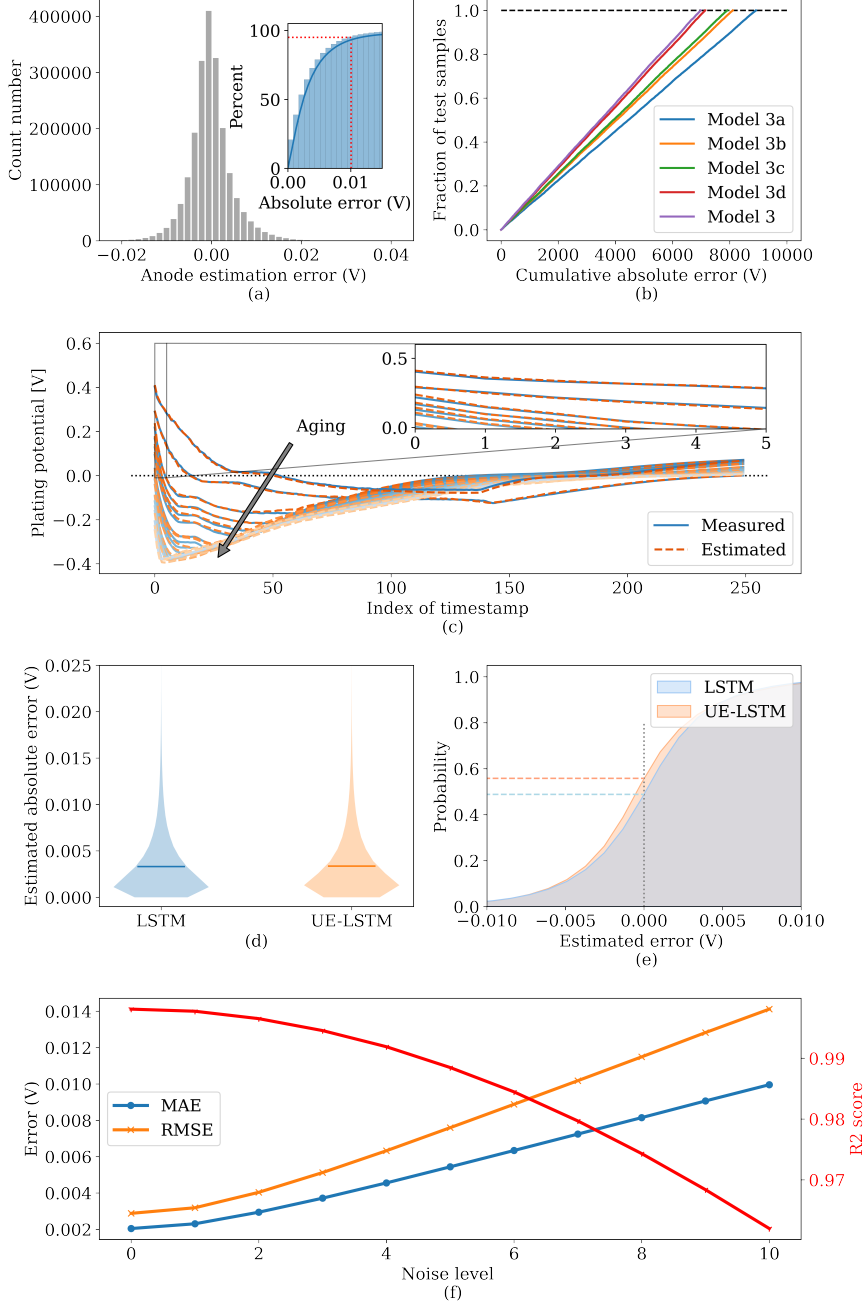


Figure 4: Estimation results for the plating potential. (a) presents the distribution of estimation errors for Model 3. (b) shows the cumulative absolute errors of Model 3 in comparison with four alternative models, each characterized by distinct input variables. (c) contrasts the plating potential estimated by Model 3 against the simulation profile for a randomly selected cell throughout its lifespan. (d) shows the violin plots of the estimation errors on the test dataset using the proposed UE-LSTM and conventional LSTM, where the horizontal lines represent the mean errors. (e) depicts the probability distribution of accumulative estimation errors using UE-LSTM and LSTM models. (f) shows the estimation errors and R^2 score for plating potential when using measurements polluted by different levels of noise.

Table 3: Estimation results of the plating potential using different feature sets.

	Feature input	MAE (mV)	RMSE (mV)
Model 3a	Current (I), Voltage (U), Temperature (T)	4.30	6.28
Model 3b	I, U, T , Capacity	3.91	5.71
Model 3c	I, U, T , Capacity, LLI	3.82	5.39
Model 3d	I, U, T , Capacity, LLI, LAM _{NE}	3.44	4.88
Model 3	I, U, T , Capacity, LLI, LAM _{PE} , LAM _{NE}	3.37	4.77

5) The effect of different levels of measurement noise. For battery applications such as EVs, the accuracy of signals measured from batteries is often reduced relative to laboratory experiments due to the need to balance sensor costs against accuracy. It is therefore crucial for the developed estimation model to possess robustness against sensor noise. For a comprehensive evaluation, we introduce ten levels of Gaussian white noise to current, voltage, and temperature measurements, with their standard deviations defined in Table 4.

The results in Fig. 4f demonstrate an almost linear increase in the estimation error with escalating levels of sensor noise. Notably, even under the most severe conditions (noise level 10, which substantially surpasses typical industry standards), our developed estimation model maintains an MAE of less than 16 mV. This finding underscores that the proposed lifelong estimation framework and its embedded Model 3 are capable of delivering accurate and robust performance in the presence of large sensor noise.

Table 4: Ten levels of Gaussian white noise introduced to measurements.

Sensor noise level	0	1	2	3	4	5	6	7	8	9	10
Current (mA)	0	5	10	15	20	25	30	35	40	45	50
Voltage (mV)	0	2.5	5	7.5	10	12.5	15	17.5	20	22.5	25
Temperature (°C)	0	0.5	1	1.5	2	2.5	3	3.5	4	4.5	5

2.7. Computational efficiency

The computational efficiency of the designed estimation algorithm, which integrates Models 1–3, is critical for enabling optimal charging control in a vehicle BMS. We have therefore assessed the computational load of our algorithm using a Nvidia Tesla A100 GPU in a Python environment. To reduce randomness in the evaluation, the algorithm is tested over ten times under identical conditions, with the mean computation times reported in Table 5.

Despite the extensive dataset used, the training process for all three developed models only requires 1060 seconds, while the testing process exhibits remarkable computational efficiency, completing in 5.27 seconds. The execution time for estimating the plating potential over a single real-world charging cycle is merely 0.16 seconds. Note that such calculations are conservative, as the three models can be executed in parallel to reduce the total required computation time. These results underscore the algorithm’s high applicability for real-world battery management.

Table 5: Computation time required by the proposed estimation algorithm.

	Computation time (s)			Data size		
	Training	Testing	Single charge	Training	Testing	Single charge
Model 1	13	0.28	0.01	7552	1888	1
Model 2	366	2.12	0.09	2.75×10^7	6.88×10^6	3645
Model 3	681	2.87	0.06	8.30×10^6	2.08×10^6	250
Total	1060	5.27	0.16			

2.8. Discussion and outlook of future research

This study demonstrates that the plating potential-controlled charging strategy can substantially extend battery lifetime and enhance charging speed. Nonetheless, uncertainties linger regarding the implications of applying high currents at the CC stage of each charge. Despite careful control to maintain a positive plating potential, the possibility for high currents to expedite aging mechanisms, aside from lithium plating, has not been fully investigated. Additionally, while using a constant control threshold to limit the onset of lithium plating has shown practical benefits in our closed-loop control system, it may not fully capture the variability of the actual plating potential in the negative electrodes. Factors such as thermal gradients, uneven particle distribution, and inhomogeneous electrodes contribute to this variability. Therefore, a slightly higher threshold of 1 mV is selected in this work to account for such variability, albeit with a small performance trade-off. Furthermore, the design of laboratory-scale three-electrode cells, with their limited surface area and metal enclosure, inherently minimizes thermal fluctuations, neglecting the impact of thermal dynamics on fast charging. These areas are critical to our understanding of battery degradation under fast charging and will be a future research direction. With the estimated plating potential, another crucial next step is to explore its usage for the development of safety- and health-conscious BMS.

3. Conclusions

This study challenges the conventional compromise between the rapid charging of Li-ion batteries and their longevity. Through experimental validation on three-electrode battery cells, we have developed a plating potential-controlled charging strategy. This strategy not only enables over 30% faster charging rates but also significantly extends battery lifespan by mitigating lithium plating, a notorious catalyst for premature battery degradation.

To adapt these laboratory findings to commercial EV batteries without a reference electrode, we introduced a novel machine learning (ML)-based framework. This framework seamlessly integrates three distinct ML models to estimate the plating potential throughout the battery's life. These models are activated selectively and intelligently based on usage scenarios, timescales of the involved system dynamics, and available data sources of the battery during real-world conditions. Specifically, Model 1 and Model 2 are designed to estimate the battery's capacity and three aging modes on a slow timescale and at low current rates, such as during destination charging. Model 3, in contrast,

operates on a fast timescale to provide real-time estimates of the plating potential during fast charging. By leveraging our newly developed UE-LSTM algorithm, time-series features from field data collected during fast charging, and non-temporal features outputted from Model 1 and Model 2, Model 3 is able to provide lifelong robust and accurate predictions under a variety of operating conditions and measurement uncertainties.

This new framework can be seamlessly integrated with existing vehicle BMS, utilizing readily available measurements. Our results represent a significant step forward in the development of more efficient and durable EV battery utilization.

4. Experimental procedures

4.1. Electrochemical battery modeling and simulation

4.1.1. SEI layer growth model

The liquid electrolyte used in Li-ion battery cells becomes unstable and reacts with lithium ions and electrons within the electrodes to form a passive solid-electrolyte interface (SEI) during charging in the first cycle, leading to around 10% capacity loss [46, 47, 48]. The SEI layer will continue to grow during battery usage, leading to capacity loss and resistance increase [49]. There are several ways to model SEI growth, as reviewed in [50]. To describe the dynamics of the SEI growth, a kinetics-limited model developed in [51] is adopted here, in which the exchange current density of the SEI-based side reactions is expressed in the Tafel equation

$$i_{\text{SEI}} = i_{0,\text{SEI}} \exp\left(\frac{\alpha nF}{RT} \eta_{\text{SEI}}\right), \quad (1)$$

$$\eta_{\text{SEI}} = U_{\text{NE}}^{\text{ref}} + \eta_{\text{NE}} - U_{\text{SEI}}^{\text{ref}}. \quad (2)$$

In (1), $i_{0,\text{SEI}}$ is the reference exchange current density, α is a transfer coefficient, n is the number of electrons participating in the reaction, F is the Faraday's constant, R is the ideal gas constant, and T represents the battery temperature. In (2), η_{SEI} is the overpotential of the SEI-based side reaction, $U_{\text{NE}}^{\text{ref}}$ is the equilibrium anode potential which is evaluated as a function of the solid phase concentration at the surface of the particle, η_{NE} is the anode overpotential, and $U_{\text{SEI}}^{\text{ref}}$ is the equilibrium potential of the SEI growth reaction, respectively.

4.1.2. LAM model

The continuous cycling of Li-ion batteries may cause electrode dissolution [41], particle cracking [52], and detachment from the binding materials [53], resulting in LAM in both the negative and positive electrodes. The volume fraction of active materials in each electrode, denoted by ϵ , can be modeled by [54, 41]

$$\frac{\partial \epsilon}{\partial t} = \beta \left(\frac{\sigma_{h,\text{max}} - \sigma_{h,\text{min}}}{\sigma_{\text{yield}}} \right)^m, \quad (3)$$

where $\sigma_{h,\text{max}}$ and $\sigma_{h,\text{min}}$ are the minimum and maximum hydraulic stress, respectively, depending on the particle radius and the average lithium concentration within the particle. The values of the parameters β , m , and σ_{yield} are often fitted from experimental data.

4.1.3. Physical parameters and simulation conditions

The SPMe-aging battery model employed in the simulation was previously parameterized against LG M50T cylindrical battery cells in [41, 50, 55, 56]. We take the parameter values from the referred references and gradually vary a set of aging-rated parameters, such as $i_{0,SEI}$ in (1) and β in (3), among different simulations. The detailed parameter values and simulation setup are given in Note 5 of the *Supplemental Information*.

Each cycle of the cell operation includes a CC-CV charge with a cut-off voltage of 4.2 V at the CC stage and a cut-off current of 50 mA at the CV stage, followed by a CC discharge with a cut-off voltage of 2.5 V. Between adjacent charge and discharge phases, a one-hour relaxation period is introduced to mimic battery behavior under calendar aging. For comprehensive coverage of diverse operating conditions encountered in real-world scenarios, the simulation incorporates various charging current rates and ambient temperatures. The simulation process is terminated if the cell has reached its end of life. Every 50 cycles, an RPT is performed to get the pseudo-OCV measurement, in which the cell is charged and discharged at 1/10C until the cut-off voltage limit of 4.2 V is reached.

4.2. ML-based battery modeling and implementation

The methods for developing the three ML models in the proposed lifelong estimation framework are introduced in this subsection.

4.2.1. KF-based fusion of ML models for capacity estimation

The methods for online capacity estimation have been well-established in the literature. A data-driven multi-model fusion method was recently developed and demonstrated high accuracy and practicability under arbitrary vehicle usage conditions [29]. We adopt it in Model 1 to estimate battery capacity continuously over the lifespan. While the details are referred to [29], we introduce the key idea here for completeness. First, a tailored set of features is meticulously curated from time-series current, voltage, and temperature measurements during battery charging. Based on these features, four distinct ML algorithms, including two probabilistic and two frequentist approaches, are applied to estimate the battery capacity. Second, leveraging usage-related histogram data, a one-step-ahead capacity prediction model is developed. In the end, a Kalman filter (KF) is utilized to systematically fuse the results of all the estimation and prediction models. The comprehensive features derived from the partial slow charging process for Model 1 are provided in Note 2 of the *Supplemental Information*.

4.2.2. LSTM for aging mode quantification

The cell OCV curve or electrochemical impedance spectroscopy (EIS) can potentially be obtained at each RPT test and used to achieve the targets of Model 2, as per [57, 58, 59]. However, for real-world EV applications, it is practically challenging to receive either reliable EIS measurements over a wide frequency range or OCV measurements over the full SoC window. In contrast, extracting a pseudo-OCV curve, e.g., during destination charging or overnight home charging, is comparatively straightforward. Thus, we formulate features from the partial charging events within an LTSM model to quantify the three aging modes as the output of Model 2.

Other than traditional neural networks (NNs) that take a single data point as the input and require manual construction of features, LSTM takes a sequence of data and performs the regression or classification without the need for feature selection and engineering. This characteristic makes LSTM well-suited for speech recognition, language translation, and robot control tasks. Considering battery applications, the collected data are usually in time series by nature. Consequently, it is suitable to use LSTM to build an estimation model. Compared to recurrent neural networks (RNNs), also designed to process time-series data, LSTM can effectively avoid vanishing gradient during training [60].

A typical LSTM unit consists of two internal cells, i.e., a memory cell c_t and a hidden cell h_t , where t represents the current time step. The memory cells can be viewed as the state that saves information over a long period of time. The hidden cell, together with the gating mechanism composed of three main gates (i.e., the input, forget, and output gates), controls the information flowing within the neural network. The detailed calculation process can be represented by the following equations [61]:

$$\begin{aligned} f_t &= \sigma(W_f x_t + U_f h_{t-1} + b_f), & i_t &= \sigma(W_i x_t + U_i h_{t-1} + b_i), \\ o_t &= \sigma(W_o x_t + U_o h_{t-1} + b_o), & \tilde{c}_t &= \tanh(W_c x_t + U_c h_{t-1} + b_c), \\ c_t &= f_t \odot c_{t-1} + i_t \odot \tilde{c}_t, & h_t &= o_t \odot \tanh(c_t), \end{aligned}$$

where x_t is the input vector, i_t , f_t , and o_t are the activation vectors of the input, forget, and output gates, respectively, and \tilde{c}_t is the memory cell's input activation vector. W and U represent the weight matrices for the input and hidden state, respectively, b is the bias term, and \odot denotes the element-wise product.

4.2.3. Alternative methods for SoH indicator estimation

Alternatively to the above approaches, two other types of approaches can be utilized to estimate the four SoH indicators. The first type is to extend the LSTM model in Section 4.2.2 to include all four SoH indicators as outputs. The second type is to extract a relevant and appropriate feature set for each SoH indicator and use them for training point-to-point ML models, such as Gaussian process regression (GPR), Bayesian regression (BR), random forest regression (RFR), and NN. A systematic comparison between the proposed approach and its two benchmarks is conducted. Illustrative results in Note 2 of the *Supplemental Information* demonstrate that the proposed approach in Section 4.2.1–4.2.2 can provide the most accurate estimation results for all the indicators, albeit with some exceptions.

4.2.4. UE-LSTM for plating potential estimation

For fast charging control based on plating potential, it is crucial to have a small safety margin so that the plating potential will not enter the negative region. Consequently, it becomes imperative to prioritize models exhibiting a tendency towards underestimation rather than overestimation, particularly as the plating potential approaches zero. To achieve this, we propose a novel algorithm, termed UE-LSTM, which employs a unique loss function J defined as follows:

$$J = \frac{1}{N} \sum_i^N J_1(i), \quad (4)$$

$$J_1(i) = \begin{cases} w_1 J_2(i), & \text{if } y_i \geq \hat{y}_i \\ J_2(i), & \text{otherwise} \end{cases} \quad (5)$$

$$J_2(i) = \begin{cases} w_2(y_i - \hat{y}_i)^2, & \text{if } |y_i| \leq 0.02 \\ (y_i - \hat{y}_i)^2, & \text{otherwise} \end{cases} \quad (6)$$

where y_i and \hat{y}_i are the true and estimated plating potential values, respectively. (5) is designed with a weighting factor $w_1 = 10$ to favor scenarios of underestimation. (6) incorporates a large weighting factor $w_2 = 50$ to improve estimation accuracy within the plating potential range of $[-0.02, 0.02]$ V.

4.2.5. Training data labeling

The capacity of the battery cell can either be directly measured during RPT tests or estimated using an accurate and reliable estimator, e.g., the one developed in [29]. As per [62], there are established methods to experimentally extract LLI information through an advanced lab setting. How to measure the LAM operando in each electrode is still an active research question. Instead, we calculate the three aging modes continuously over the battery's life using pseudo-OCV measurements and the diagnostic algorithm of [63] (see Note 1 of the *Supplemental Information* for details).

4.3. Evaluation matrices

The MAE and RMSE are used to quantify the estimation performance for the four considered SoH indicators. These two evaluation matrices are defined as

$$MAE = \frac{1}{N} \sum_{i=1}^N (y_i - \hat{y}_i) \quad (7)$$

$$RMSE = \sqrt{\frac{1}{N} \sum_{i=1}^N (y_i - \hat{y}_i)^2} \quad (8)$$

where N represents the total number of samples in the test set, y_i and \hat{y}_i are the true value and the estimated value, respectively, and i is the time step. For the plating potential estimation, in addition to the MAE and RMSE, the coefficient of determination is used to evaluate how well the model fits the test samples, as defined by

$$R^2 = 1 - \frac{\sum_{i=1}^N (y_i - \hat{y}_i)^2}{\sum_{i=1}^N (y_i - \bar{y})^2}, \quad (9)$$

where the average estimated value $\bar{y} = \frac{1}{N} \sum_{i=1}^N \hat{y}_i$.

4.4. Resource availability

4.4.1. Data availability

The raw cycling data for the three-electrode battery cells can be found at:

(<https://drive.google.com/file/d/1hkryupdtkwx4bfooIwDW0linKfkywi5c/view?usp=sharing>)

Declaration of generative AI and AI-assisted technologies in the writing process

During the preparation of this work, the authors used ChatGPT4 to polish the language. After using this tool, the authors reviewed and edited the content as needed and took full responsibility for the content of the publication.

References

- [1] Zero emission vehicles: first fit for 55 deal will end the sale of new co2 emitting cars in europe by 2035, https://ec.europa.eu/commission/presscorner/detail/en/ip_22_6462, accessed: 05-July-2023 (2022).
- [2] B. Nykvist, M. Nilsson, Rapidly falling costs of battery packs for electric vehicles, *Nat. Clim. Change* 5 (4) (2015) 329–332.
- [3] M. S. Ziegler, J. E. Trancik, Re-examining rates of lithium-ion battery technology improvement and cost decline, *Energy Environ. Sci.* 14 (4) (2021) 1635–1651.
- [4] N. Wassiliadis, M. Steinsträter, M. Schreiber, P. Rosner, L. Nicoletti, F. Schmid, M. Ank, O. Teichert, L. Wildfeuer, J. Schneider, et al., Quantifying the state of the art of electric powertrains in battery electric vehicles: Range, efficiency, and lifetime from component to system level of the volkswagen id. 3, *Etransportation* 12 (2022) 100167.
- [5] N. Wassiliadis, J. Schneider, A. Frank, L. Wildfeuer, X. Lin, A. Jossen, M. Lienkamp, Review of fast charging strategies for lithium-ion battery systems and their applicability for battery electric vehicles, *J. Energy Storage* 44 (2021) 103306.
- [6] C.-Y. Wang, T. Liu, X.-G. Yang, S. Ge, N. V. Stanley, E. S. Rountree, Y. Leng, B. D. McCarthy, Fast charging of energy-dense lithium-ion batteries, *Nature* 611 (7936) (2022) 485–490.
- [7] G. K. Peprah, T. Wik, Y. Huang, F. Altaf, C. Zou, Control-oriented 2D thermal modelling of cylindrical battery cells for optimal tab and surface cooling, in: *American Control Conference*, IEEE, 2024, pp. 1–6.
- [8] A. Tomaszewska, Z. Chu, X. Feng, S. O’kane, X. Liu, J. Chen, C. Ji, E. Endler, R. Li, L. Liu, et al., Lithium-ion battery fast charging: A review, *ETransportation* 1 (2019) 100011.
- [9] I. Aghabali, J. Bauman, P. J. Kollmeyer, Y. Wang, B. Bilgin, A. Emadi, 800-v electric vehicle powertrains: Review and analysis of benefits, challenges, and future trends, *IEEE Trans. Electrif.* 7 (3) (2020) 927–948.
- [10] E. J. Dufek, D. P. Abraham, I. Bloom, B.-R. Chen, P. R. Chinnam, A. M. Colclasure, K. L. Gering, M. Keyser, S. Kim, W. Mai, et al., Developing extreme fast charge battery protocols—a review spanning materials to systems, *J. Power Sources* 526 (2022) 231129.
- [11] M. Li, M. Feng, D. Luo, Z. Chen, Fast charging li-ion batteries for a new era of electric vehicles, *Cell Rep. Phys. Sci.* 1 (10) (2020).
- [12] W. Xie, X. Liu, R. He, Y. Li, X. Gao, X. Li, Z. Peng, S. Feng, X. Feng, S. Yang, Challenges and opportunities toward fast-charging of lithium-ion batteries, *J. Energy Storage* 32 (2020) 101837.
- [13] J. Sieg, J. Bandlow, T. Mitsch, D. Dragicevic, T. Materna, B. Spier, H. Witzenhausen, M. Ecker, D. U. Sauer, Fast charging of an electric vehicle lithium-ion battery at the limit of the lithium deposition process, *J. Power Sources* 427 (2019) 260–270.
- [14] N. Wassiliadis, J. Kriegler, K. A. Gamra, M. Lienkamp, Model-based health-aware fast charging to mitigate the risk of lithium plating and prolong the cycle life of lithium-ion batteries in electric vehicles, *J. Power Sources* 561 (2023) 232586.
- [15] T. Waldmann, B.-I. Hogg, M. Wohlfahrt-Mehrens, Li plating as unwanted side reaction in commercial Li-ion cells—a review, *J. Power Sources* 384 (2018) 107–124.

- [16] T. R. Tanim, P. P. Paul, V. Thampy, C. Cao, H.-G. Steinrück, J. N. Weker, M. F. Toney, E. J. Dufek, M. C. Evans, A. N. Jansen, et al., Heterogeneous behavior of lithium plating during extreme fast charging, *Cell Rep. Phys. Sci.* 1 (7) (2020).
- [17] X. Lu, M. Lagnoni, A. Bertei, S. Das, R. E. Owen, Q. Li, K. O'Regan, A. Wade, D. P. Finegan, E. Kendrick, et al., Multiscale dynamics of charging and plating in graphite electrodes coupling operando microscopy and phase-field modelling, *Nat. Commun.* 14 (1) (2023) 5127.
- [18] J. Sieg, A. U. Schmid, L. Rau, A. Gesterkamp, M. Storch, B. Spier, K. P. Birke, D. U. Sauer, Fast-charging capability of lithium-ion cells: Influence of electrode aging and electrolyte consumption, *Appl. Energy* 305 (2022) 117747.
- [19] T. Amietszajew, E. McTurk, J. Fleming, R. Bhagat, Understanding the limits of rapid charging using instrumented commercial 18650 high-energy Li-ion cells, *Electrochim. Acta* 263 (2018) 346–352.
- [20] Y. Hoshi, Y. Narita, K. Honda, T. Ohtaki, I. Shitanda, M. Itagaki, Optimization of reference electrode position in a three-electrode cell for impedance measurements in lithium-ion rechargeable battery by finite element method, *J. Power Sources* 288 (2015) 168–175.
- [21] S. J. An, J. Li, C. Daniel, S. Kalnaus, D. L. Wood, Design and demonstration of three-electrode pouch cells for lithium-ion batteries, *J. Electrochem. Soc.* 164 (7) (2017) A1755.
- [22] Y. Lu, X. Han, Z. Chu, X. Feng, Y. Qin, M. Ouyang, L. Lu, A decomposed electrode model for real-time anode potential observation of lithium-ion batteries, *J. Power Sources* 513 (2021) 230529.
- [23] M. Doyle, T. F. Fuller, J. Newman, Modeling of galvanostatic charge and discharge of the lithium/polymer/insertion cell, *J. Electrochem. Soc.* 140 (6) (1993) 1526.
- [24] F. Ringbeck, M. Garbade, D. U. Sauer, Uncertainty-aware state estimation for electrochemical model-based fast charging control of lithium-ion batteries, *J. Power Sources* 470 (2020) 228221.
- [25] L. Li, Y. Ren, K. O'Regan, U. R. Koleti, E. Kendrick, W. D. Widanage, J. Marco, Lithium-ion battery cathode and anode potential observer based on reduced-order electrochemical single particle model, *J. Energy Storage* 44 (2021) 103324.
- [26] M. Andersson, M. Streb, J. Y. Ko, V. L. Klass, M. Klett, H. Ekström, M. Johansson, G. Lindbergh, Parametrization of physics-based battery models from input–output data: A review of methodology and current research, *J. Power Sources* 521 (2022) 230859.
- [27] A. M. Bizeray, J.-H. Kim, S. R. Duncan, D. A. Howey, Identifiability and parameter estimation of the single particle lithium-ion battery model, *IEEE Trans. Control Syst. Technol.* 27 (5) (2018) 1862–1877.
- [28] W. Li, M. Rentemeister, J. Badeda, D. Jöst, D. Schulte, D. U. Sauer, Digital twin for battery systems: Cloud battery management system with online state-of-charge and state-of-health estimation, *J. Energy Storage* 30 (2020) 101557.
- [29] Y. Zhang, T. Wik, J. Bergström, C. Zou, State of health estimation for lithium-ion batteries under arbitrary usage using data-driven multimodel fusion, *IEEE Trans. Transp. Electrif.* 10 (1) (2024) 1494–1507.
- [30] Y. Zhang, T. Wik, J. Bergström, M. Pecht, C. Zou, A machine learning-based framework for online prediction of battery ageing trajectory and lifetime using histogram data, *J. Power Sources* 526 (2022) 231110.
- [31] Z. Wei, X. Yang, Y. Li, H. He, W. Li, D. U. Sauer, Machine learning-based fast charging of lithium-ion battery by perceiving and regulating internal microscopic states, *Energy Stor. Mater.* 56 (2023) 62–75.
- [32] X. Lin, Real-time prediction of anode potential in li-ion batteries using long short-term neural networks for lithium plating prevention, *J. Electrochem. Soc.* 166 (10) (2019) A1893.
- [33] J. C. Hamar, S. V. Erhard, C. Zoerr, A. Jossen, Anode potential estimation in lithium-ion batteries using data-driven models for online applications, *J. Electrochem. Soc.* 168 (3) (2021) 030535.
- [34] S. Ahmed, I. Bloom, A. N. Jansen, T. Tanim, E. J. Dufek, A. Pesaran, A. Burnham, R. B. Carlson, F. Dias, K. Hardy, et al., Enabling fast charging—a battery technology gap assessment, *J. Power Sources* 367 (2017) 250–262.
- [35] P. Arora, M. Doyle, R. E. White, Mathematical modeling of the lithium deposition overcharge reaction in lithium-ion batteries using carbon-based negative electrodes, *J. Electrochem. Soc.* 146 (10) (1999) 3543.
- [36] C. Uhlmann, J. Illig, M. Ender, R. Schuster, E. Ivers-Tiffée, In situ detection of lithium metal plating on graphite in experimental cells, *J. Power Sources* 279 (2015) 428–438.
- [37] X. Lin, K. Khosravinia, X. Hu, J. Li, W. Lu, Lithium plating mechanism, detection, and mitigation in lithium-ion batteries, *Prog. Energy*

- Combust. Sci. 87 (2021) 100953.
- [38] T. Gao, Y. Han, D. Fraggedakis, S. Das, T. Zhou, C.-N. Yeh, S. Xu, W. C. Chueh, J. Li, M. Z. Bazant, Interplay of lithium intercalation and plating on a single graphite particle, Joule 5 (2) (2021) 393–414.
- [39] J. S. Edge, S. O’Kane, R. Prosser, N. D. Kirkaldy, A. N. Patel, A. Hales, A. Ghosh, W. Ai, J. Chen, J. Yang, et al., Lithium ion battery degradation: what you need to know, Phys. Chem. Chem. Phys. 23 (14) (2021) 8200–8221.
- [40] S. J. Moura, F. B. Argomedo, R. Klein, A. Mirtabatabaei, M. Krstic, Battery state estimation for a single particle model with electrolyte dynamics, IEEE Trans. Control Syst. Technol. 25 (2) (2016) 453–468.
- [41] S. E. O’Kane, W. Ai, G. Madabattula, D. Alonso-Alvarez, R. Timms, V. Sulzer, J. S. Edge, B. Wu, G. J. Offer, M. Marinescu, Lithium-ion battery degradation: how to model it, Phys. Chem. Chem. Phys. 24 (13) (2022) 7909–7922.
- [42] X.-G. Yang, C.-Y. Wang, Understanding the trilemma of fast charging, energy density and cycle life of lithium-ion batteries, J. Power Sources 402 (2018) 489–498.
- [43] Y. Zhang, X. Li, L. Su, Z. Li, B. Y. Liaw, J. Zhang, Lithium plating detection and quantification in Li-ion cells from degradation behaviors, ECS Trans. 75 (23) (2017) 37.
- [44] V. Sulzer, S. G. Marquis, R. Timms, M. Robinson, S. J. Chapman, Python Battery Mathematical Modelling (PyBaMM), J. Open Res. Softw. 9 (1) (2021) 14.
- [45] H. Ruan, J. Chen, W. Ai, B. Wu, Generalised diagnostic framework for rapid battery degradation quantification with deep learning, Energy AI 9 (2022) 100158.
- [46] J. Vetter, P. Novák, M. Wagner, C. Veit, K.-C. Möller, J. Besenhard, M. Winter, M. Wohlfahrt-Mehrens, C. Vogler, A. Hammouche, Ageing mechanisms in lithium-ion batteries, J. Power Sources 147 (1) (2005) 269–281.
- [47] M. Broussely, P. Biensan, F. Bonhomme, P. Blanchard, S. Herreyre, K. Nechev, R. Staniewicz, Main aging mechanisms in Li ion batteries, J. Power Sources 146 (1-2) (2005) 90–96.
- [48] Y. Gao, J. Jiang, C. Zhang, W. Zhang, Z. Ma, Y. Jiang, Lithium-ion battery aging mechanisms and life model under different charging stresses, J. Power Sources 356 (2017) 103–114.
- [49] P. Bai, J. Li, F. R. Brushett, M. Z. Bazant, Transition of lithium growth mechanisms in liquid electrolytes, Energy Environ. Sci. 9 (10) (2016) 3221–3229.
- [50] J. M. Reniers, G. Mulder, D. A. Howey, Review and performance comparison of mechanical-chemical degradation models for lithium-ion batteries, J. Electrochem. Soc. 166 (14) (2019) A3189–A3200.
- [51] X.-G. Yang, Y. Leng, G. Zhang, S. Ge, C.-Y. Wang, Modeling of lithium plating induced aging of lithium-ion batteries: Transition from linear to nonlinear aging, J. Power Sources 360 (2017) 28–40.
- [52] F. M. Kindermann, J. Keil, A. Frank, A. Jossen, A sei modeling approach distinguishing between capacity and power fade, J. Electrochem. Soc. 164 (12) (2017) E287.
- [53] X. Zhang, W. Shyy, A. M. Sastry, Numerical simulation of intercalation-induced stress in li-ion battery electrode particles, J. Electrochem. Soc. 154 (10) (2007) A910.
- [54] I. Laresgoiti, S. Käbitz, M. Ecker, D. U. Sauer, Modeling mechanical degradation in lithium ion batteries during cycling: Solid electrolyte interphase fracture, J. Power Sources 300 (2015) 112–122.
- [55] C.-H. Chen, F. B. Planella, K. O’Regan, D. Gastol, W. D. Widanage, E. Kendrick, Development of experimental techniques for parameterization of multi-scale lithium-ion battery models, J. Electrochem. Soc. 167 (8) (2020).
- [56] J. Sturm, A. Rheinfeld, I. Zilberman, F. Spingler, S. Kosch, F. Frie, A. Jossen, Modeling and simulation of inhomogeneities in a 18650 nickel-rich, silicon-graphite lithium-ion cell during fast charging, J. Power Sources 412 (2019) 204–223.
- [57] C. Pastor-Fernández, K. Uddin, G. H. Chouchelamane, W. D. Widanage, J. Marco, A comparison between electrochemical impedance spectroscopy and incremental capacity-differential voltage as Li-ion diagnostic techniques to identify and quantify the effects of degradation modes within battery management systems, J. Power Sources 360 (2017) 301–318.
- [58] C. Pastor-Fernández, T. F. Yu, W. D. Widanage, J. Marco, Critical review of non-invasive diagnosis techniques for quantification of degrada-

- tion modes in lithium-ion batteries, *Renewable Sustainable Energy Rev.* 109 (2019) 138–159.
- [59] R. Xiong, Y. Pan, W. Shen, H. Li, F. Sun, Lithium-ion battery aging mechanisms and diagnosis method for automotive applications: Recent advances and perspectives, *Renewable Sustainable Energy Rev.* 131 (2020) 110048.
- [60] R. Pascanu, T. Mikolov, Y. Bengio, On the difficulty of training recurrent neural networks, in: *International conference on machine learning*, Pmlr, 2013, pp. 1310–1318.
- [61] S. Hochreiter, J. Schmidhuber, Long short-term memory, *Neural Comput.* 9 (8) (1997) 1735–1780.
- [62] Y. Fang, A. J. Smith, R. W. Lindström, G. Lindbergh, I. Furó, Quantifying lithium lost to plating and formation of the solid-electrolyte interphase in graphite and commercial battery components, *Appl. Mater. Today* 28 (2022) 101527.
- [63] C. R. Birkl, M. R. Roberts, E. McTurk, P. G. Bruce, D. A. Howey, Degradation diagnostics for lithium ion cells, *J. Power Sources* 341 (2017) 373–386.